NANO LETTERS

2007
Vol. 7, No. 5
1352−1359

Submicrometer In-Plane Integrated Surface Plasmon Cavities

J.-C. Weeber,* A. Bouhelier, G. Colas des Francs, L. Markey, and A. Dereux

Institut Carnot de Bourgogne, UMR 5209 CNRS-Université de Bourgogne, 9 avenue A. Savary, BP 47870, F-21078 Dijon, France

Received February 20, 2007; Revised Manuscript Received April 2, 2007

ABSTRACT

The optical properties of in-plane integrated surface plasmon polariton (SPP) cavities comprised of a thin film area sandwiched between two one-dimensional Bragg SPP mirrors are investigated numerically and experimentally. We discuss the resonance condition of these cavities, and we analyze in details the physical origin of the dispersion of this resonance. On the basis of numerical results, we show that in-plane SPP cavities can be used to achieve local SPP field enhancement and antireflecting SPP layers. The numerical results are compared to near-field optical images recorded by operating a photon scanning tunneling microscope. From the near-field images recorded over cavities with different sizes at different frequencies, we verify the resonance condition obtained numerically and we measure the quality factor of a submicrometer in-plane integrated SPP cavity.

Surface plasmon polaritons (SPPs) originating from the collective oscillations of conduction electrons at the surface of a metal are exploited for decades for sensing purposes.[1] All SPP-based sensors rely on the perturbation of the SPP excitation due to an absorbate present at the surface of the metallic structures sustaining the plasmon mode (either localized or delocalized). Recently, coupling between light emitters and surface plasmon modes has been considered in detail. For example, modification of quantum wells or quantum dot luminescence[2,3] or improvement of the yield of light emitting diodes mediated by SPP modes have been reported.[4−6] These examples show that SPP−matter interaction is of paramount importance not only for sensing applications but also for the development of SPP-based active optical devices. In this respect, structures aimed at confining, localizing, or enhancing SPP fields deserve a careful examination as they could be used to increase SPP−matter interaction or to restrict this interaction to a well-controlled area. The capability of microfabrication techniques to texture at the submicrometer scale thin metal films has raised much interest for SPP modes supported by in-plane integrated nanostructures. Among others, structures such as nanoholes engraved in metal films or metal nanoparticles deposited on a substrate have been used to achieve for example local SPP sources,[7,8] optical SPP Bragg mirrors,[9−11] or plasmonic crystals.[12−15] SPP Bragg mirrors are of particular interest because they can be used as building blocks of more sophisticated SPP devices such as interferometers or beam splitters.[16] Typical SPP Bragg mirrors are comprised of metal ridges with a period that depends upon the frequency and on the incidence angle for which the mirror is designed. In analogy with the local modes created by introducing a defect into the stack of a standard Bragg mirror, a SPP cavity can be created by enlarging one of the periods of the mirror. Despite the importance of this device for the applications cited above, there are to date only a few theoretical and experimental works dedicated to the study of in-plane integrated SPP cavities. The numerical modeling of large in-plane SPP cavities comprised of dielectric scatterers deposited on a loss-less metal has been performed using Green's tensor based formalism in ref 17. SPP cavities used as virtual scanning near-field optical microscope probes are proposed in ref 18 and are studied numerically using a Fourier based method. The same kind of cavities are studied in the context of quantum electrodynamic applications in ref 19. In-plane integrated SPP cavities engraved into metal films have been found to be efficient to confined SPP[20] or to modify the emission pattern of a nanohole used as a pointlike light source.[21] However to date, a systematic study of these cavities and in particular of their resonance condition is still lacking.

The goal of this work is to investigate both numerically and experimentally in-plane integrated SPP cavities consisting of a thin film area surrounded by two one-dimensional (1D) Bragg mirrors of finite size. By using a grating formalism, we first analyzed the resonance condition of these types of cavities. We discuss in particular the physical origin of the dispersion of this resonance condition. In order to verify our numerical results, SPP cavities have been microfabricated by using electron beam lithography. A near-field optical microscope is operated to observe the spectral response of cavities with different sizes. On the basis of these

10.1021/nl070403y CCC: $37.00
Published on Web 04/18/2007

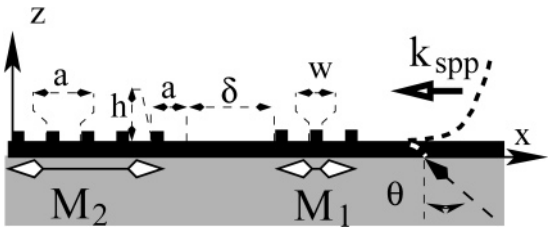

Figure 1. Schematic view of the in-plane integrated SPP cavities. The cavities are comprised of a thin film area with a total length $a + \delta$ sandwiched between two one-dimensional Bragg mirrors.

near-field optical images, we demonstrate the resonance of in-plane integrated cavities and we measure the quality factor of a submicrometer cavity.

Figure 1 shows a diagram of the in-plane integrated SPP cavities we consider in this work. The cavities consist of a thin film area surrounded by two finite-size SPP mirrors M_1 and M_2. The two mirrors consist of one-dimensional microgratings of metal ridges with a period a lying on a metal thin film. The metal thin film is deposited on a transparent glass substrate. The length of the cavity is characterized by the parameter δ representing the excess of size of the cavity as compared to a standard mirror period. In other words, an unperturbed period of the Bragg mirror corresponds to $\delta = 0$. The reason for this definition of the cavity size will become clear later. We consider a TM-polarized plane wave (electric field parallel to the plane of incidence) traveling in the glass substrate (index n_1) toward the positive values of z and falling on the thin film at an angle of incidence θ. With the appropriate θ, the metal/superstrate (air, $n_3 = 1.0$) SPP is launched at the top interface of the thin film and interacts with the cavity. To characterize the resonance condition of the cavity, we need to compute the near-field intensity distribution over cavities of different sizes. For that purpose, we use the differential method (DM) which is a Fourier expansion based grating formalism.[22−24] For a 1D grating with a period d illuminated in planar diffraction (plane of incidence perpendicular to the ridges) the complete set of electromagnetic field components can be expressed from the single tangential component H_y. In the substrate and superstrate, this component can be written as a Floquet expansion

$$H_y^{(j)}(x,z) = \sum_{m=-N}^{+N} H(m)_y^{(j)} \exp i(\alpha_m x + \gamma_m^{(j)} z) \qquad (1)$$

where the superscript (j) can be either (1) or (3) and refers to the homogeneous medium in which the field is considered and where $2N+1$ is the total number of harmonics used to expand the electromagnetic field. The x and z wavevector components of each plane wave in the Floquet expansion are respectively given by

$$\alpha_m = n_1 k_0 \sin\theta + m\frac{2\pi}{d}$$

$$\gamma_m^{(j)} = \sqrt{(n^{(j)}k_0)^2 - \alpha_m^2} \qquad (2)$$

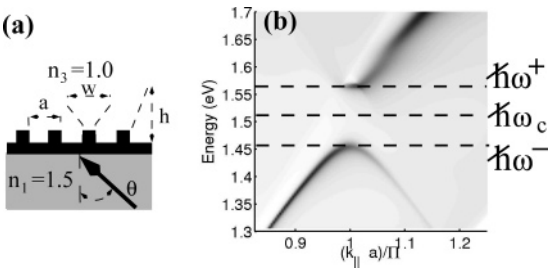

Figure 2. (a) Computational situation for the calculation of the reflectivity of a gold thin film (thickness 50 nm) textured by a one-dimensional grating of square gold ridges ($a = 390$ nm, $W = h = 40$ nm). (b) Reflectivity of the textured thin film (gray scale from $R = 0.4$ (black) to $R = 1$ (white)). A band gap opens up at the boundary of the first Brillouin zone. The low-frequency gap edge, the central frequency, and the high band gap edge correspond to free-space wavelengths of 849, 821, and 790 nm, respectively.

where $k_0 = (2\pi/\lambda_0)$ is the modulus of the incident wavevector in vacuum and where m is an integer. Depending on the α_m, $\gamma_m^{(j)}$ can be either pure real or pure imaginary (with $n^{(j)}$ real) introducing respectively progressive or evanescent waves in the Floquet expansion. The sign of the imaginary part of $\gamma_m^{(i)}$ must be chosen positive for $\gamma_m^{(3)}$ and negative for $\gamma_m^{(1)}$ in order to prevent the existence of antievanescent waves in the expansion. The use of the DM for modeling metal gratings has been prohibited for a long time because of numerical instabilities. This problem has been solved about 10 years ago by using the stable so-called S-matrix algorithm.[25] This algorithm leads to the computation of the scattering matrix S of the grating which connects the Fourier amplitudes of the field in the substrate (medium (1)) and in the superstrate (medium (3)) according to the following matrix equation

$$\begin{bmatrix} H_y^{(1)\mathrm{d}}(m) \\ H_y^{(3)\mathrm{u}}(m) \end{bmatrix} = \begin{pmatrix} S_{11} & S_{12} \\ S_{21} & S_{22} \end{pmatrix} \begin{bmatrix} H_y^{(3)\mathrm{d}}(m) \\ H_y^{(1)\mathrm{u}}(m) \end{bmatrix} \qquad (3)$$

where the superscripts u and d in the Fourier amplitudes $H_y^{(i)}(m)$ denote respectively waves traveling in the upward ($z > 0$) and downward ($z < 0$) directions. In the incident medium, the only wave traveling upward is the incident one and then $H_y^{(1)\mathrm{u}}(m) = H_y^{\mathrm{inc}}\delta_{m,0}$ where H_y^{inc} is the amplitude of incident magnetic field and where $\delta_{0,m}$ denotes the Kronecker symbol. In the substrate, the downward-traveling waves can be interpreted as reflected waves whereas in the superstrate, the upward-traveling waves correspond to transmitted ones. Because in our case the incident field propagates upward, the outgoing wave condition implies that all the components $H_y^{(3)\mathrm{d}}(m)$ are zero for all values of m. From these remarks it can be readily seen that S-matrix blocks S_{22} and S_{12} correspond respectively to a transmission and reflection matrix. The computation of the S-matrix requires the numerical integration of the Maxwell equations projected onto the plane waves basis within a thin layer of the grating. It is worth to mention that in order to improve the convergence of the Floquet field expansions, our implementation of the DM takes into account Li's remarks about the

truncated Fourier transform of the product of discontinuous functions.[26−28] Once the S-matrix of the grating is known, the electromagnetic field can be computed from the plane wave expansion at any observation point in the superstrate or substrate.

We start our numerical analysis by the characterization of an unperturbed Bragg mirror. We consider the infinitely extended grating shown in Figure 2a. The grating consists of gold ridges with a square cross section ($W = h = 40$ nm) lying on a gold film with a thickness of 50 nm. The period a of the grating is chosen to be 390 nm in order to create a gap in the dispersion curve of the SPP at a frequency corresponding roughly to a wavelength in vacuum of 800 nm.[11] In order to investigate the SPP excitation, we compute the reflectivity R of the periodically textured thin film. With the DM, the computation of R is straightforward and is given by

$$R = \sum_{\hat{m}} |H_y^{(1)\mathrm{d}}(\hat{m})|^2 \frac{\gamma^{(1)}(\hat{m})}{\gamma^{(1)}(0)} \qquad (4)$$

where the sum is taken over the whole set of Fourier components in the field expansion corresponding to propagative homogeneous plane waves in the substrate and where $\gamma^{(1)}(0)$ is the z-component of the incident wavevector. The result of the computation of the modulated thin film reflectivity for different frequencies and angles of incidence is shown in Figure 2b. This calculation has been performed with a number of plane waves ($N = 15$) in the Floquet expansions large enough to obtain stable values of the reflectivity over the frequency range we consider. For this calculation and for all subsequent numerical results, we use the dielectric function of gold tabulated in ref 29. The low reflectivity points (dark areas) reveal the SPP excitation, and as expected, a gap in the dispersion curve of the SPP opens up at the boundary of the first Brillouin zone. The gap has a width of about 110 meV and is centered at $\hbar\omega_c = 1.51$ eV (821 nm). The high- and low-frequency band gap edges (denoted $\hbar\omega^+$ and $\hbar\omega^-$ in Figure 2b) correspond to energies of 1.57 eV (790 nm) and 1.46 eV (849 nm), respectively. On the basis of this result, we conclude that such SPP mirrors can be used to build SPP cavities for a wavelength range centered around a free-space wavelength of 820 nm.

Let us consider now the in-plane SPP cavity shown schematically in Figure 3a and consisting of a mirror M_1 with 10 periods and a mirror M_2 with 35 periods. The two micrograting constituting the cavity lie on a thin gold film (thickness 50 nm) excited in the Kretschmann−Raether configuration. The SPP launched at the top interface of the thin film propagates from the right to the left. The DM can only be used to compute the field scattered by periodic objects; therefore the cavity we consider is repeated periodically with a period d. A period $d = 90$ μm about three times larger than the (1/e) damping distance $L_{(1/e)}$ of thin SPP at the low band gap edge frequency ω^- is used for the following computations in order to prevent significant interactions between two adjacent cavities ($L_{(1/e)} = 34$ μm for a 50 nm thick gold film at $\lambda_0 = 850$ nm). With such a period, the SPP scattered by a given cavity reaches the next one with an amplitude divided by a factor larger than 20. Because the period d is much larger than the period $a = 0.390$ μm of the Bragg mirrors, the number of plane waves in the Floquet expansion must be large enough to take into account the high spatial frequencies of the object. We find that a number of $2N + 1 = 1601$ plane waves is sufficient since no significant change of the numerical results is observed with either $2N + 1 = 1401$ or $2N + 1 = 1701$. Parts b, c, and d of Figure 3 displayed the electric near-field intensity profiles (normalized with respect to the incident electrical intensity $|E_{\mathrm{inc}}|^2$) computed along an observation line located 80 nm over the

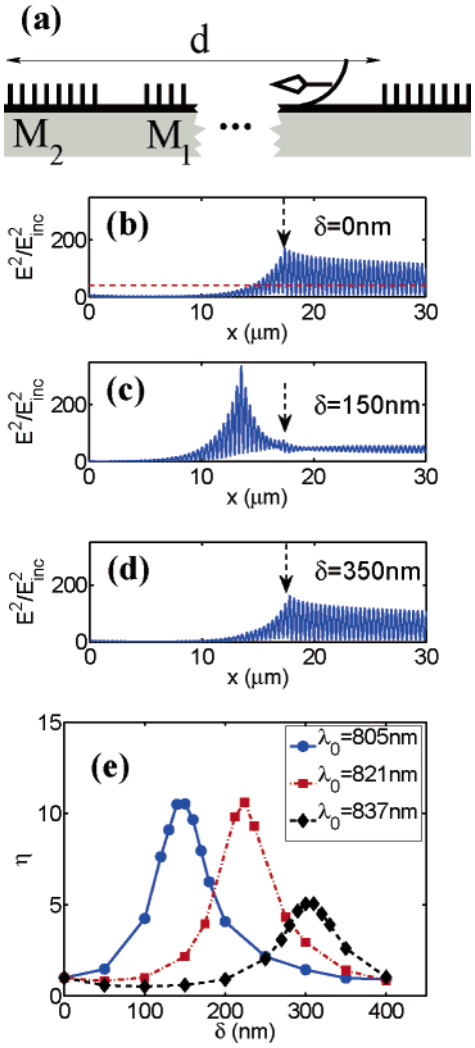

Figure 3. (a) Computational situation for the calculation of the near-field profiles over a single in-plane integrated SPP cavity. The period d of the system is 90 μm and a SPP launched at the thin film top interface is traveling from the right to the left. (b, c, and d) Near-field profiles computed over cavities with respective sizes of $\delta = 0$, $\delta = 150$, and $\delta = 350$ nm. The last element of mirror M_2 corresponds to $x = 0.0$ μm whereas the dashed arrow shows the location of the first element of mirror M_1. In (b), the dashed line shows the electric field intensity of a SPP excited on the top interface of the bare thin film with the illumination conditions of the cavities. (e) Computation of the intensity enhancement as a function of the cavity size for different incident free-space wavelengths.

top of the mirrors, for cavity sizes of $\delta = 0$, 150, and 350 nm, respectively. On each of these figures, the textured thin film area extends from $x = 0$ to the vertical dashed arrow showing the location of the beginning of mirror M_1. These near-field profiles have been obtained for an incident frequency corresponding to a free-space wavelength of $\lambda_0 = 805$ nm and an angle of incidence of 43°. For $\delta = 0$ nm, the cavity is simply a Bragg mirror and accordingly we observe a very neat standing wave pattern in the area where the incident and the back-reflected SPP interact. Inside the mirror, the near-field profile exhibits an exponential decay as expected for a frequency within the gap.[30] The peak intensity of the standing wave pattern being close to four times the intensity of the bare thin film SPP (excited with the same illumination conditions), we conclude that the reflectivity of a 45 periods mirror is close to 100%. For $\delta = 150$ nm, the near-field profile exhibits a rather weakly contrasted standing wave pattern in front of M_1 and a large peak at the location of the cavity suggesting that the cavity is resonant. On the contrary, for $\delta = 350$ nm, the near-field profile is very similar to that of the unperturbed mirror. In order to characterize more quantitatively the resonance of the cavity, we compute the enhancement η given by

$$\eta = \frac{\int_{\Omega} E^2_{\text{cavity}}(x)\,dx}{\int_{\Omega} E^2_{\text{mirror}}(x)\,dx} \tag{5}$$

where $E^2_{\text{cavity}}(x)$ and $E^2_{\text{mirror}}(x)$ denote the near-field intensity over the cavity and over the unperturbed mirror, respectively, and where Ω is the x-range (with a total length of $a + \delta$) corresponding to the location of the cavity. Thus, the ratio η characterizes the enhancement of the field at the location of the cavity compared to the field at the same location when the mirror is unperturbed. The enhancement η has been computed for different values of δ and different wavelengths. The results are shown in Figure 3e. For δ ranging from 0 to 400 nm, a single peak is observed for the three wavelengths 805, 821, and 837 nm. The peak position shifts toward large values of δ when the incident energy decreases from $\hbar\omega^+$ (790 nm) to $\hbar\omega^-$ (849 nm). In addition, we observe that the enhancement η at $\lambda_0 = 837$ nm is half the enhancement obtained for the two wavelengths $\lambda_0 = 821$ nm and $\lambda_0 = 837$ nm. This dramatic damping of the enhancement cannot be attributed to the increase of the resonant cavity size for increasing incident wavelengths since such a damping does not occur when switching from $\lambda_0 = 805$ nm to $\lambda_0 = 821$ nm. In fact, the small value of η at 837 nm is more likely related to the Bragg mirror efficiency when the incident energy approaches the low-energy band gap edge. Indeed, if we measure the (1/e) damping distance of the SPP intensity propagating inside the mirror, we find respectively 2.05, 2.20, and 3.4 μm for $\lambda_0 = 805$, 821, and 837 nm, respectively. The large inner-mirror SPP damping distance at $\lambda_0 = 837$ nm leading simultaneously to a large normalization value for the computation of η and to a small number of SPP round trips into the cavity, the enhancement *eta* is found to be rather small when the incident wavelength is close to the mirror long-wavelength band edge.

To understand the increase of the resonant cavity size for increasing incident wavelengths, we consider the resonance condition of an in-plane integrated SPP cavity. The resonance of such a cavity occurs if the field of the SPP undergoes an integer number of 2π phase shifts after a round trip into the cavity. For a cavity with a linear size $a + \delta$, the total phase shift of the SPP field after a round trip can be written (see Figure 4a)

$$\Delta\Phi = 2k_{\text{spp}}(a + \delta) + \Phi_r^{(1)} + \Phi_r^{(2)} \tag{6}$$

where $k_{\text{spp}} = (2\pi/\lambda_{\text{spp}})$ is the modulus of the SPP wavevector and where $\Phi_r^{(1)}$ and $\Phi_r^{(2)}$ are the phase shift at the reflection on the mirrors M_1 and M_2. Assuming that the two mirrors are similar, the cavity will be resonant if

$$k_{\text{spp}}(a + \delta) + \Phi_r = m\pi \tag{7}$$

with m an integer. For frequencies in the gap, the period a of the grating is almost equal to $(\lambda_{\text{spp}}/2)$; therefore the resonance condition becomes

$$k_{\text{spp}}\delta + \Phi_r \simeq m\pi \tag{8}$$

The reflection phase shift Φ_r is a priori unknown; however we can assess the value of this phase shift if we consider the electric field intensity distribution of the SPP modes at ω^+ and ω^-. As shown schematically in Figure 4b, for a grating with a vanishing small modulation, the SPP mode at ω^- exhibits an electric field intensity distribution in phase with the topography of the grating whereas the near-field intensity profile of the SPP mode at ω^+ is π-phase-shifted with respect to that topography.[31] If we assume a finite size grating, a SPP incident on this grating at ω^+ or ω^- will couple to the corresponding SPP Bloch mode. We suppose that the boundary between the flat thin film and the grating is located at x_L (see Figure 4b), then at any observation points (x_L,z) in the superstrate the field must be continuous leading to the following expression

$$E_{\text{Bloch}}(x_L,z,\omega^{(+,-)}) = E^{\text{inc}}_{\text{spp}}(x_L,z,\omega^{(+,-)}) + E^{\text{R}}_{\text{spp}}(x_L,z,\omega^{(+,-)})\exp(i\Phi_R\omega^{(+,-)}) \tag{9}$$

where E_{Bloch} stands for the electric field of the SPP Bloch mode and where $E^{\text{inc}}_{\text{spp}}$ and $E^{\text{R}}_{\text{spp}}$ are the incident and reflected SPPs, respectively, traveling along the flat thin film. From eq 9, we can conclude that the reflection phase shift at ω^- must be equal to $\Phi_R(\omega^-) = 0$ (2π) in such a way that the standing wave pattern created by the interference of the incident and reflected field exhibits a maximum at x_L. Using the same argument, one can see that the incident and the reflected field must be π phase shifted at ω^+ leading to $\Phi_R(\omega^+) = \pi$ (2π) . For symmetry reasons, the reflection phase shift at the central gap frequency ω_c is expected to be

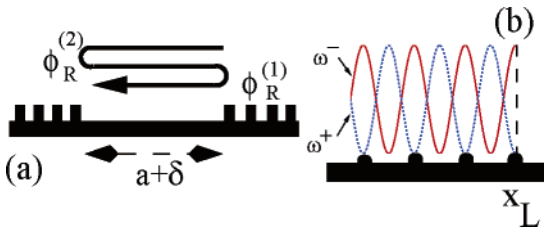

Figure 4. (a) Schematic view of a round trip of the SPP into the cavity. The phase change after a round-trip must account for the reflection phase shift of the SPP field on Bragg mirrors M_1 and M_2. (b) Schematic view of the SPP Bloch modes electric field intensity distributions at the low-frequency ω^- and high-frequency ω^+ band gap edges.

$\Phi_R(\omega_c) = (\pi/2)\ (2\pi)$ such that the resonance condition of the cavity is given by

$$\delta > (2k+1)\frac{\lambda_{spp}}{4}, \quad \text{if} \quad \omega^- < \omega < \omega_c$$

$$\delta = (2k+1)\frac{\lambda_{spp}}{4}, \quad \text{if} \quad \omega = \omega_c \qquad (10)$$

$$\delta < (2k+1)\frac{\lambda_{spp}}{4}, \quad \text{if} \quad \omega_c < \omega < \omega^+$$

In particular, if the incident frequency approaches ω^- (ω^+) by upper values (lower values), the resonance condition is given by δ approaching $m(\lambda_{spp}/2)$ (with m an integer) by lower (upper) values. This conclusion explains the numerical results displayed in Figure 3e. Indeed, for $\lambda_0 = 821$ nm (central gap wavelength), we find that the resonance occurs at $\delta = 224$ nm which is only 20 nm different from what is expected from the theoretical resonance condition given by eq 10 when $\omega = \omega_c$. For an incident free-space wavelength of 805 nm ($\omega > \omega_c$), the reflection phase shift is expected to be larger than ($\pi/2$) and accordingly the size of the resonant cavity ($\delta = 150$ nm) is smaller than that for the central gap frequency. Note that the effective index $n_{eff} = (\lambda_0/\lambda_{spp})$ of the SPP cannot be at the origin of the dispersion of the resonance condition since it changes by only 10^{-3} for a free-space wavelength varying from 821 to 805 nm. Finally, for a free-space wavelength of 837 nm located in the low-frequency part of the band gap, the reflection phase is smaller than ($\pi/2$) leading to a size of the resonant cavity larger than that for the central gap frequency. As shown by the contrast of the standing-wave pattern visible in Figure 3c, when the cavity is resonant the SPP is only poorly back-reflected. This implies that the cavity acts in this case as an SPP *anti-reflecting* layer. This analogy is even clearer when considering the central gap frequency since, in this case, the resonance condition is strictly similar to the antireflecting condition by a homogeneous thin film coating.[32]

The computations discussed above have been performed using SPP mirrors consisting of micrograting with a rather small duty cycle (W/a) = 10%. From a practical viewpoint, such a duty cycle is somewhat difficult to obtain because it requires the fabrication of very narrow ridges. It is then of practical interest to investigate the influence of this structural parameter on the resonance condition. For that purpose, we have computed the enhancement factor η for cavities designed using Bragg mirrors with the same period $a = 390$ nm but with two different widths of the ridges $W = 40$ nm and $W = 120$ nm. The results of this computation for an incident free-space wavelength of 805 nm are shown in parts a and b of Figure 5, respectively. For δ ranging from 0 to 1.2 μm, we observe three resonances corresponding to $\delta =$ 150, 550, and 950 nm for the two values of W. The values of δ corresponding to the resonances are separated, as expected, by a distance of roughly ($\lambda_{spp}/2$) leading to an extra phase shift of 2π after a round trip into the cavity. From this computation, we show that the width of the ridges W does not influence significantly the resonance condition of the cavities. This result can be understood by considering the physical origin of the Bragg reflection. The first-order SPP Bragg reflection occurs because of the momentum transfer mediated by the Fourier harmonic of the grating profile with a spatial frequency of ($2\pi/a$). In direct space, this particular harmonic corresponds to a sinusoïdal grating profile with a period a and having an amplitude that depends upon the duty cycle of the original grating. Thus, with this equivalent sinusoïdal grating, the SPP traveling into the cavity experienced a cavity size of $a + \delta$ instead of the actual size of $a + \delta - W$ (see Figure 5c). The latter remark explains also why we find in our case a resonance condition similar to the one obtained when the Bragg mirrors consist of sinusoidal gratings (at least at the center gap frequency)[18] provided that the definition of δ corresponds to the excess of size of the cavity as compared to an unperturbed period.

The resonance of the cavities has been characterized so far by means of the enhancement factor η for which the reference situation is an unperturbed mirror. However, to be useful for improving SPP−matter interaction, the cavities should be able to enhance the SPP field as compared to the SPP field excited on a bare thin film. Parts d−f of Figure 5 show the near-field intensity distributions computed at a distance of 20 nm over the resonant cavities with $W = 40$ nm (Figure 5a). These profiles show the near-field electric intensity normalized by the electric intensity of the SPP excited on a bare gold thin film with the same illumination conditions than for the cavities. For increasing cavity sizes, we observe an increasing number of peaks in the near-field profiles revealing the excitation of increasing cavity mode orders. For the smallest size ($\delta = 150$ nm), we find that the electric intensity is enhanced by an order of magnitude compared to that of a thin film. This rather modest enhancement can be due to the fact that the reflectivity of the entrance mirror M_1 is not maximum in our case. In fact, in the configuration we consider in this work, the cavities are excited by an incident SPP that is first transmitted through the entrance mirror. As a result a perfectly reflecting mirror cannot be used for M_1. Note, however, that if a light emitter is located into the cavity, larger enhancement is expected because in this case both mirrors M_1 and M_2 can be chosen to have maximum reflectivity. The profiles displayed in parts d−f of Figure 5 show that, unlike loss-less cavities, the SPP

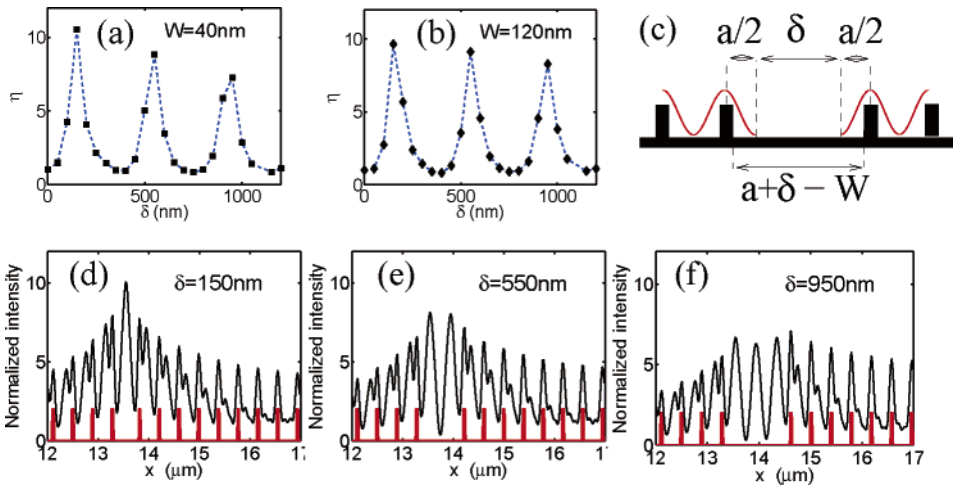

Figure 5. (a and b) Near-field intensity enhancement over cavities with increasing sizes and two different widths of the gold ridges. The incident free-space wavelength is 805 nm. For the two ridge widths $W = 40$ nm and $W = 120$ nm, the resonances occur at $\delta = 150$, $\delta = 550$, and $\delta = 950$ nm. (c) Schematic view of the cavity size experienced by the SPP explaining the physical origin of the small impact of W on the size of the resonant cavities. (d, e, and f) Near-field electrical intensity profiles computed 20 nm over the top of the cavity. The near-field intensity is normalized with respect to that of a SPP excited an a bare thin film.

intensity enhancement (as compared to that of a bare thin film) depends upon the cavity mode order. In this case, the damping of the intensity enhancement with the cavity order occurs because of the increase of the cavity size. By using a model of cavity comprised of two hard-wall mirrors with finite reflectivities leading to intensity enhancement similar to that observed in Figure 5d and assuming a bare thin film SPP bouncing between these two mirrors, it can be shown that the intensity enhancement inside the cavity is about two times less impacted by an increase of the cavity size (corresponding to half the SPP wavelength) than in the case of the in-plane integrated cavities. Therefore, from this result we conclude that although the SPP mode bouncing between the two Bragg mirrors must have a phase constant close to that of a bare thin film, its attenuation constant is necessarily larger than the attenuation of the thin film mode.

To confirm our numerical results, we have microfabricated in-plane integrated SPP cavities using electron-beam lithography. The mirrors constituting the cavities have been first designed on an ITO-doped glass substrate and eventually coated with a thermally evaporated gold thin film (thickness = 53 nm). Our experimental cavities consist of finite-size gold lines gratings (period a=385 nm, height $h = 44$ nm, width $W = 110$ nm) covered with a gold thin film. The sample has been glued on the hypotenuse of a right angle BK7-glass prism by means of an index matching oil and illuminated in the Kretschmann−Raether configuration by using a collimated TM-polarized titanium−sapphire laser beam. The angle of incidence corresponding to the top interface SPP resonance has been adjusted by minimizing the reflectivity of the thin film. The characterization of the SPP cavities has been performed using a photon scanning tunneling microscope (PSTM) equipped with chromium-coated glass fiber tips. A detailed description of the experimental setup used in this work can be found in ref 33. The scanning electron microscope (SEM) images and the corresponding PSTM images of an unperturbed mirror and

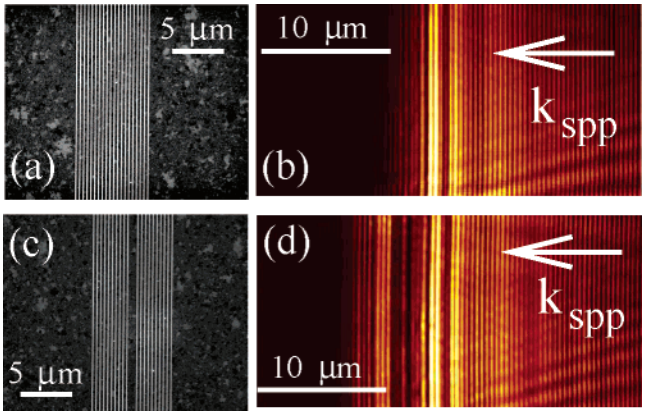

Figure 6. (a and b) SEM and PSTM images of an unperturbed Bragg mirror. The incident free-space wavelength is 805 nm and the incident SPP travels from the right to the left. (c and d) SEM and PSTM image of an in-plane integrated SPP cavity with a size $\delta = 550$ nm. Mirrors M_1 and M_2 surrounding the cavity are both comprised of 10 gold lines. A significant field enhancement (as compared to the unperturbed mirror) is visible on image d at the location of the cavity.

a SPP cavity are displayed in Figure 6. When illuminated with a free-space wavelength of 805 nm, a neat standing wave pattern resulting from the interference of the incident (traveling from the right to the left) and back-reflected SPP is visible on the PSTM image of the unperturbed mirror (Figure 6b). The incident frequency is expected to be in the gap of the grating, and accordingly the SPP intensity decays abruptly within the mirror. When a cavity with a size $\delta = 550$ nm is sandwiched between two 10-line mirrors the PSTM image (Figure 6d) displays again a very contrasted standing wave pattern. However a clear enhancement of the near-field intensity at the location of the cavity is also observed, suggesting that the cavity is resonant. To confirm this result, PSTM images of two other cavities with respective sizes of $\delta = 750$ nm and $\delta = 940$ nm were recorded. The SEM images of the reference mirror and the three

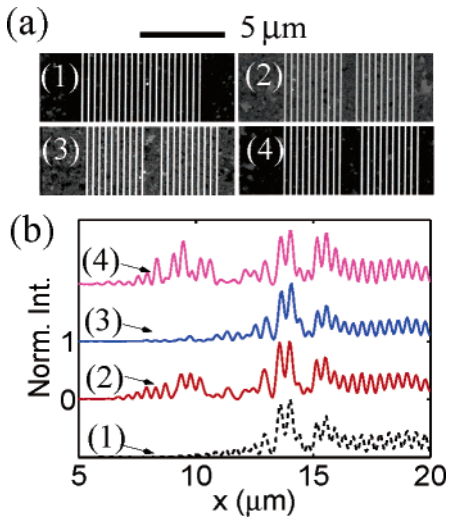

Figure 7. (a) SEM images of cavities with different sizes. Labels 1, 2, 3, and 4 correspond to $\delta = 0$, $\delta = 550$, $\delta = 750$, and $\delta = 940$ nm, respectively. (b) Average longitudinal near-field intensity profiles recorded at 805 nm over the different cavities. Each profile is normalized with respect to its maximum intensity. The profiles have been translated vertically for clarity.

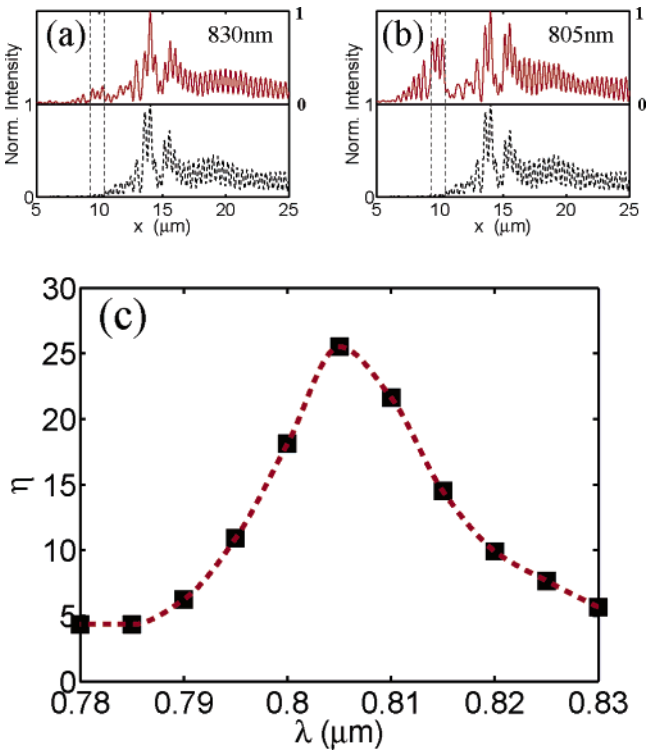

Figure 8. (a) (solid) Near-field profile recorded over the cavity with a size $\delta = 550$ nm for an incident free-space wavelength of 830 nm. (dashed) Near-field profile recorded at 805 nm over an unperturbed reference mirror. (b) Same as (a) except that near-field profile (solid line) is recorded at 805 nm. (c) Enhancement of the near-field intensity over the cavity as a function of the incident wavelength. (The dashed line is a guide to the eyes.)

different cavities considered are shown in Figure 7a. The near-field profiles displayed in Figure 7b have been obtained by averaging up to 20 longitudinal cross-cuts of the PSTM images of each cavity. In this figure, the dashed profile corresponds to the unperturbed mirror whereas profiles labeled 2, 3, and 4 are respectively obtained for increasing cavity sizes $\delta = 550$, $\delta = 750$, and $\delta = 940$ nm. In agreement with the numerical results displayed in parts a and b of Figure 5, we observe that the cavities leading to a significant intensity enhancement correspond to $\delta = 550$ and $\delta = 940$ nm whereas for $\delta = 750$ nm, the near-field profile is only slightly different from that of the reference mirror, as expected for an off-resonance cavity. On the basis of these experimental results, we conclude that our numerical procedure is reliable to model the resonance of an in-plane SPP cavity. It should be noted however that unlike the numerical results, the contrast of the standing wave pattern visible in front of the resonant cavities is almost the same as that for the unperturbed mirror or the off-resonant cavity. In addition, on the experimental profiles of the resonant situations, the maximum field intensity inside the cavity is not much larger than the SPP intensity over the thin film as is the case in Figure 3c for example. These two behaviors can be understood from a larger reflectivity of the entrance mirror M_1 for the experimental cavities than for the numerical ones. Accordingly, for an increasing M_1 reflectivity, the amplitude of the SPP transmitted through this mirror decreases as well as the maximum intensity inside the cavity. Moreover, if the amplitude of the SPP reflected by mirror M_1 is much larger than the amplitude of the SPP reflected by M_2 (after a round trip into the cavity and a double transmission through M_1), the antireflecting effect discussed previously (see Figure 3c) is not visible anymore. Indeed, this antireflecting effect is only efficient provided that the SPP amplitudes reflected by M_1 and M_2 are quite close since it relies on the destructive interference of these two SPPs.

To complete the characterization of the SPP cavities, we investigate the quality factor of the resonance observed for $\delta = 550$ nm. To estimate this quality factor, we swept the incident free-space wavelength from 780 to 830 nm by 5 nm steps. For each frequency, a PTSM image of the cavity was recorded and near-field profiles were extracted according to the procedure described above. The near-field profiles obtained for $\lambda_0 = 830$ nm and $\lambda_0 = 805$ nm are shown in the top portion of parts a and b of Figure 8, respectively. The enhancement η of the near-field intensity over the cavity for each frequency was experimentally determined according to eq 5 where the reference profile is that of the unperturbed mirror at 805 nm (shown in the bottom portion of parts a and b of Figure 8). Figure 8c shows the experimental enhancement η plotted as a function of the incident free-space wavelength. In agreement with the numerical results, we find that the cavity with $\delta = 550$ nm is resonant at 805 nm. However, the enhancement at $\lambda_0 = 805$ nm is significantly larger than the enhancement obtained numerically. This result is one more time consistent with a reflectivity of the experimental mirrors larger than in the numerical situation. Indeed, in this case, the damping of the SPP inside the experimental unperturbed mirror is larger than in the numerical case and accordingly the reference intensity used in the calculation of η is smaller in the experimental situation than in the theoretical one. However it is likely that the

discrepancy between numerical and experimental values of η is also due to the contribution of out-of-plane scattered light to the PSTM signal when a resonant cavity is imaged. By measuring the full width at half-maximum $\Delta\lambda_0^{fwhm}$ of the enhancement peak, we find a quality factor of the resonance of $Q = (\Delta\lambda_0^{fwhm}/\lambda_0^{res}) = 45$. This rather poor quality factor (as compared to that of a dielectric cavity) could however be exploited to improve the spectral selectivity of SPP Bragg filters. Indeed although demonstrated for long-range SPP,[34] narrow-band filters for interface SPP are still lacking.

In summary, we have investigated numerically and experimentally in-plane integrated SPP cavities consisting of a thin film area sandwiched between two 1D SPP Bragg mirrors. On the basis of numerical results obtained with the DM, we have explicitly given the resonance condition of these cavities and discussed the origin of the resonance dispersion. In particular, we have shown that for the central gap frequency of the Bragg mirrors used to build the cavities, the resonance is achieved provided that the cavity size is an odd number of quarter-SPP wavelength. We have also shown that resonant in-plane integrated cavities may be of practical interest for enhancing SPP field or for designing "anti-reflecting" SPP layers. The numerical results have been compared to near-field images of SPP cavities microfabricated by electron-beam lithography. Good agreement between the experimental and the numerical sizes of the resonant cavities has been observed. Finally, by sweeping the incident frequency, we have demonstrated that a quality factor of a few tens can be achieved with in-plane integrated SPP cavities. Despite this rather low quality factor, direct applications of the resonant cavities can be anticipated for improving the spectral selectivity of SPP filters.

Acknowledgment. This work was supported by the European Commission (Project EC FP6 IST STREP PLASMOCOM) and the Regional Council of Burgundy (ARCEN project). The authors acknowledge also Professor J.-J. Greffet for fruitful discussions.

References

(1) Homola, J.; Yee, S. S.; Gauglitz, G. *Sens. Actuators, B* **1999**, *54*, 3.
(2) Okamoto, K.; Nini, I.; Shvartser, A.; Narukawa, Y.; Mukai, T.; Scherer, A. *Nat. Mater.* **2004**, *3*, 601.
(3) Biteen, J. S.; Lewis, N. S.; Atwater, H.; Mertens, H.; Polman, A. *Appl. Phys. Lett.* **2006**, *88*, 131109.
(4) Barnes, W. L. *J. Lightwave Technol.* **1999**, *17*, 2170.
(5) Yates, C. J.; Samuel, D. W.; Burn, P. L.; Wedge, S.; Barnes, W. L. *Appl. Phys. Lett.* **2006**, *88*, 161105.
(6) Parta, P. A.; Harries, M.; Summers, H. D. *Appl. Phys. Lett.* **2006**, *89*, 121120.
(7) Egorov, D.; Dennis, B. S.; Blumberg, G.; Haftel, M. I. *Phys. Rev. B* **2004**, *70*, 033404.
(8) Devaux, E.; Ebbesen, T. W.; Weeber, J.-C.; Dereux, A. *Appl. Phys. Lett.* **2003**, 83, 4936.
(9) Ditlbacher, H.; Krenn, K. R.; Schider, G.; Leitner, A.; Aussenegg, F. R. *Appl. Phys. Lett.* **2002**, *81*, 1762.
(10) Drezet, A.; Stephanov, A. L.; Ditlbacher, H.; Hohenau, A.; Aussenegg, F. R.; Leitner, A.; Krenn, J. R. *Appl. Phys. Lett.* **2005**, *86*, 074104.
(11) Gonzalez, M.-U.; Weeber, J.-C.; Baudrion, A.-L.; Stephanov, A. L.; Devaux, E.; Ebbesen, T. W. *Phys. Rev. B* **2006**, *73*, 155416.
(12) Kitson, S. C.; Barnes, W. L.; Sambles, J. R. *Phys. Rev. Lett.* **1996**, *77*, 2670.
(13) Bozhevolnyi, S. I.; Erland, J.; Leosson, K.; Skovgaard, P. M. W.; Hvam, J. M. *Phys. Rev. Lett.* **2001**, *86*, 3008.
(14) Baudrion, A.-L.; Weeber, J.-C.; Dereux, A.; Lecamp, G.; Lalanne, P. *Phys. Rev. B* **2006**, *74*, 125406.
(15) Weeber, J.-C.; Baudrion, A.-L., Bouhelier, A.; Bruyant, A.; Colas des Francs, G.; Zia, R.; Dereux, A. *Appl. Phys. Lett.* **2006**, *89*, 211109.
(16) Weeber, J.-C., Gonzalez, M.-U.; Baudrion, A.-L.; Dereux, A. *Appl. Phys. Lett.* **2005**, *87*, 221101.
(17) Pincemin, F.; Greffet, J.-J. *J. Opt. Soc. Am. A* **1996**, *13*, 1499.
(18) Deserovi, E.; Paeder, V.; Vaccaro, L.; Herzig, H.-P. *Opt. Express* **2005**, *13*, 7017.
(19) Gong, Y.; Vuckovic, J. *Appl. Phys. Lett.* **2007**, *90*, 033113.
(20) Steele, J. M.; Liu, Z.; Wang, Y.; Zang, X. *Opt. Express* **2006**, *14*, 5664.
(21) Lezec, H. J.; Degiron, A.; Devaux, E.; Linke, R. A.; Martin-Moreno, L.; Garcia-Vidal, F. J.; Ebbesen, T. W. *Science* **2002**, *297*, 820.
(22) Nevière, M.; Popov, E.; *Light propagation in periodic media, Differential theory and design*; Marcel Dekker, Inc.: Basel, 2003.
(23) Montiel, F.; Nevière, M. *J. Opt. Soc. Am. A* **1994**, *11*, 3241.
(24) Popov, E.; Bozhkov, B. *Appl. Opt.* **2000**, *39*,4926.
(25) Li, L. *J. Opt. Soc. Am. A* **1996**, *13*, 1024.
(26) Li, L. *J. Opt. Soc. Am. A* **1997**, *10*, 2758.
(27) Lalanne, P.; Morris, G. M. *J. Opt. Soc. Am. A* **1996**, *13*, 779.
(28) Granet, G.; Guizal, B. *J. Opt. Soc. Am. A* **1996**, *13*, 1019.
(29) Palik, E. *Handbook of Optical Constants of Solids*; Academic Press, Inc.: London, 1985.
(30) Yariv, A.; Yeh, P. *Optical waves in crystals*; Wiley-Interscience: Hoboken, NJ, 2003.
(31) Barnes, W. L.; Preist, T. W.; Kitson, S. C.; Sambles, J. R. *Phys. Rev. B* **1996**, *54*, 6227.
(32) Born, M.; Wolf, E. *Principles of Optics*; Pergamon Press: Oxford, 1984.
(33) Weeber, J.-C.; Krenn, J.-R.; Dereux, A.; Lamprecht, B.; et al. *Phys. Rev. B* **2001**, *64*, 045411.
(34) Jette-Charbonneau, S.; Charbonneau, R.; Lahoud, N.; Mattiussi, G. A.; Berini, P. *IEEE J. Quantum Electron.* **2005**, *41*, 1480.

NL070403Y